Lay Description

Examining internal anatomical features of animals without affecting their original characteristics has long been a challenge for zoologists. In this respect, X-ray computed tomography has recently become a valuable non-invasive tool for visualising internal structures without the necessity of sectioning the specimen. While the imaging of mineralized structures such as the skeleton does not constitute a problem for computed tomography, differentiating between soft materials like specific tissues is more problematic and commonly requires treatment of the sample with specific staining agents. Several contrasting approaches have been applied in computed tomography studies, but investigations of their effect on different tissue types, especially in soft-bodied animals are scarce. In our study, we used a high-resolution imaging technique known as synchrotron radiation-based X-ray micro-computed tomography to demonstrate the effects of several contrasting approaches on the imaging of different tissue types of Onychophora (velvet worms), a small group of soft-bodied invertebrates relevant for studying animal evolution. We have compared the effects of the tested approaches both qualitatively (i.e., visually) in two dimensions as well as quantitatively (i.e., numerically), in order to infer the most suitable method for studying these animals. Even though our results suggest that the best contrasting approach largely depends on the type of structure or tissue of interest, the overview presented herein suggests that X-ray micro-computed tomography is a promising technique for studying onychophorans and might help researchers to address some of the many evolutionary questions surrounding this animal group.

Evaluation of contrasting techniques for X-ray imaging of velvet worms (Onychophora)

Henry Jahn[1,*], Ivo de Sena Oliveira[1, 2], Vladimir Gross[1], Christine Martin[1], Alexander Hipp[3], Georg Mayer[1] & Jörg U. Hammel[3, 4]

[1]Department of Zoology, Institute of Biology, University of Kassel, Heinrich-Plett-Straße 40, D-34132 Kassel, Germany.

[2]Departamento de Zoologia, Instituto de Ciências Biológicas, Universidade Federal de Minas Gerais, Av. Antônio Carlos 6627, 31270-901 Belo Horizonte, Brazil.

[3]Institute of Materials Research, Helmholtz-Zentrum Geesthacht, Max-Planck-Str. 1, D-21502 Geesthacht, Germany.

[4]Institut für Spezielle Zoologie und Evolutionsbiologie mit Phyletischem Museum, Friedrich-Schiller-University of Jena, Erbertstr. 1, D-07743 Jena, Germany.

*Corresponding author (email: *henry.jahn@uni-kassel.de, Tel: +49 561 804-4380; Fax: +49 561 804-4800*)

Short title: X-ray imaging of onychophorans

Keywords: Invertebrate morphology, quantitative analyses, soft tissue contrast, box plot analyses, 3D imaging, SR-µCT

Summary

Non-invasive imaging techniques like X-ray computed tomography have become very popular in zoology, as they allow for simultaneous imaging of the internal and external morphology of organisms. Nevertheless, the effect of different staining approaches required for this method on samples lacking mineralized tissues, such as soft-bodied invertebrates, remains understudied. Herein, we used synchrotron radiation-based X-ray micro-computed tomography to compare the effects of commonly used contrasting approaches on onychophorans — soft-bodied invertebrates important for studying animal evolution. Representatives of *Euperipatoides rowelli* were stained with osmium tetroxide (vapour or solution), ruthenium red, phosphotungstic acid, or iodine. Unstained specimens were imaged using both standard attenuation-based and differential phase-contrast setups to simulate analyses with museum material. Our comparative qualitative analyses of several tissue types demonstrate that osmium tetroxide provides the best overall tissue contrast in onychophorans, whereas the remaining staining agents rather favour the visualisation of specific tissues and/or structures. Quantitative analyses using signal-to-noise ratio measurements show that the level of image noise may vary according to the staining agent and scanning medium selected. Furthermore, box-and-whisker plots revealed substantial overlap in grey values among structures in all datasets, suggesting that a combination of semi-automatic and manual segmentation of structures is required for comprehensive 3D reconstructions of Onychophora, irrespective of the approach selected. Our results show that X-ray micro-computed tomography is a promising technique for studying onychophorans and, despite the benefits and disadvantages of different staining agents for specific tissues/structures, this method retrieves informative data that may eventually help address evolutionary questions long associated with Onychophora.

Introduction

Non-invasive X-ray computed tomography (=CT) methods have recently become popular for studying animal morphology and development (e.g., Hammel *et al.*, 2009; Friedrich *et al.*, 2013; Handschuh *et al.*, 2013; Blanke *et al.*, 2014; Pendar *et al.*, 2015; Weihmann *et al.*, 2015). This is because, in contrast to other imaging techniques, CT has the advantage of simultaneously accessing internal and external anatomical details of virtually any organism. Moreover, it allows three-dimensional reconstruction of individual organs and tissues — a process called segmentation (Pham *et al.*, 2000). A number of CT setups have been commonly used in zoological studies, including computed tomography instruments designed for medical purposes, laboratory-based micro-computed tomography (=µCT) devices and synchrotron radiation-based X-ray micro-computed tomography (=SR-µCT) stations (Mizutani & Suzuki, 2012). Although the spatial resolution of laboratory-based CT devices has improved substantially (up to 400 nm) in the last few years, SR-µCT remains unmatched due to its unlimited source of highly brilliant X-rays, which allows CT scans with comparable spatial but higher density resolution (Kirz & Jacobsen, 2009; Falcone *et al.*, 2011; Dierick *et al.*, 2014; Greving *et al.*, 2014).

Irrespective of the setup, CT methods applied to biological samples produce images based on the different absorption coefficients of tissues, organs, and structures of an organism, i.e., how prone these structures are to penetration by the X-ray beam (Hounsfield, 1973). In this respect, imaging hard tissue structures such as bones, shells, or chitinous structures is rarely a problem using CT techniques, while discriminating between soft tissues is a more difficult task. Obtaining CT information from soft tissue, however, can be facilitated by treating samples with different staining agents prior to analyses. Among the staining agents commonly used are osmium tetroxide (=OsO_4), phosphotungstic acid solution (=PTA), or ruthenium red (=RR) — substances that interact at different structural levels with organs and tissues and confer them characteristic attenuation coefficients, thus allowing for their

identification and discrimination by contrast in CT datasets. Since these staining agents have different properties , selecting an appropriate contrasting approach becomes a critical step for imaging organisms that lack hard structures, such as any soft-bodied invertebrate (Metscher, 2009a, b; Kerbl *et al.*, 2013; Fernández *et al.*, 2014).

Among various groups of soft-bodied invertebrates, onychophorans, or velvet worms (Fig. 1A), play an important role in understanding animal evolution. This can be credited to their ancient origin, conserved morphology, and key phylogenetic position as closely related to the arthropods — the world's largest and most diverse animal group (e.g., Mayer *et al.*, 2015a; Mayer, 2016; Martin *et al.*, 2017a). In particular, onychophorans are pivotal for understanding intricate evolutionary processes underlying the successful radiation of arthropods, such as arthropodisation (evolution of jointed limbs), arthrodisation (evolution of body sclerotisation), tagmatisation (fusion of body segments into functional units) and establishment of a specialized ganglionated nervous system (Martin *et al.*, 2017a). Even though onychophorans have never been investigated comprehensively by CT techniques, recent studies suggested that this method is promising for studying their anatomy and may eventually help to shed light on evolutionary questions that remain unanswered (Mayer *et al.*, 2015b; Müller *et al.*, 2017).

The CT data currently available for Onychophora are still very limited and restricted to their jaws (Mayer *et al.*, 2015b) and selected leg muscles (Müller *et al.*, 2017). While the onychophoran jaws are sclerotized structures easily visualised in CT scans and the leg musculature has been imaged using a prototype nanoCT device with sample size constraints, the question now arises of whether or not CT techniques could also have a broader application for Onychophora. For example, it is unclear whether or not the different types of soft tissues in Onychophora can be discriminated using contrasting approaches commonly described in the literature and whether or not the latter would also allow the segmentation of these tissues for detailed 3D reconstructions. On one hand, a literature survey reveals that several

contrasting approaches, have been successfully applied to different soft-bodied invertebrates such as bryozoans, lumbricid annelids, and caudofoveate and cephalopod molluscs (Metscher, 2009a, b; Kerbl *et al.*, 2013; Fernández *et al.*, 2014). On the other hand, it is still uncertain, which approach favours the imaging of which tissue type and especially, which approach would provide the clearest distinction between tissues when applied to onychophorans.

Finally, previous comparative studies revealed that besides qualitative data, quantitative analyses are also important for identifying a suitable contrasting approach for a specific animal group (Metscher, 2009a; Swart *et al.*, 2016). Such analyses assess the grey value distribution within selected regions of the CT dataset and reveal how likely structures and tissues are to be automatically recognized and distinguished from each other using software tools for segmentation. This is particularly relevant for zoological samples given the complexity of most organ systems, e.g., musculature or nervous systems, in which case fully manual segmentation is extremely time-consuming even for small samples.

In order to address the issues above and contribute to future CT studies on Onychophora, we present herein a qualitative and quantitative comparison of CT datasets obtained from representatives of the onychophoran species *Euperipatoides rowelli* (Fig. 1A) subjected to six different staining approaches and analysed using SR-µCT. In addition, we simulated the analyses of museum material, to which staining methods typically cannot be applied, by scanning unstained specimens with two different SR-µCT setups. The effects of the tested approaches on different tissues and organs are herein demonstrated qualitatively by comparing two-dimensional (2D) visualisations of corresponding virtual sections (Fig. 1B) and quantitatively by using box-and-whisker plot analyses and signal-to-noise ratio measurements. Furthermore, we discuss methodological issues that may arise when previously established CT protocols are applied to specimens of Onychophora. The results of our study demonstrate that the staining method plays an important role in the visualisation and

segmentation of structures in Onychophora and suggest that the selection of an appropriate contrasting approach will largely depend on the target tissue.

Material and Methods

Specimens, fixations and contrast stains

Specimens of *Euperipatoides rowelli* Reid, 1996 (Onychophora, Peripatopsidae) were collected from decaying logs and leaf litter in the Tallaganda State Forest, New South Wales, Australia (35°30'31"S, 149°36'14.3"E, 934 m) and kept in culture under constant conditions as previously described (Baer & Mayer, 2012). Specimens were collected and exported under the collection permit number SPPR0008 issued by the Forestry Commission of New South Wales and the export permit number WT2012-8163 obtained from the Department of Sustainability, Environment, Water, Population and Communities, respectively. A total of eight specimens were used for this study; each specimen was subjected to a different fixation/contrasting method commonly applied in CT studies (Table 1). Seven specimens were anaesthetized in chloroform vapour for 10–15 s. One specimen was directly exposed to osmium tetroxide vapour (OsO_4, 4%, Carl Roth GmbH & Co. KG, Karlsruhe, Germany). All specimens were fixed overnight in either glutaraldehyde (2.5% in 0.1 M sodium cacodylate buffer) or paraformaldehyde (PFA; 4% in 0.1 M phosphate buffered saline [=PBS]), washed several times in the corresponding buffer, and processed further as follows.

With the exception of the specimen exposed to OsO_4 vapour and two additional ones that were left unstained, the remaining specimens were submitted to four different treatments as follows: (i) two specimens were initially stained in 2% OsO_4 overnight and subsequently washed several times in the corresponding buffer solution; (ii) one specimen was dehydrated through an ethanol series (up to 70%) and stained for 5 days in phosphotungstic acid (=PTA) solution (Carl Roth GmbH & Co. KG; 0.3% in 70% ethanol); (iii) one specimen was stained overnight in ruthenium red (=RR) solution (Carl Roth GmbH & Co. KG; 60 mg in 20 ml of

2.5% glutaraldehyde in cacodylate buffer solution); and (iv) one specimen was dehydrated through an ethanol series, placed overnight in 1% iodine solution (in absolute ethanol) and washed several times in absolute ethanol.

Thereafter, all specimens were dehydrated further in an ethanol series up to absolute ethanol. Two specimens previously stained with OsO_4 and iodine, respectively, were embedded in Araldite® (Huntsman Advanced Materials, Basel, Switzerland) as previously described (Mayer, 2006a). One unstained specimen was kept in absolute ethanol for differential phase-contrast analyses to simulate a typical museum specimen. The six remaining animals were critical point dried using a CPD 010 (Balzers, Liechtenstein) to avoid potential emergence of gas bubbles resulting from the interaction of liquids with the high photon flux at the synchrotron radiation source as well as to achieve higher contrast. The nomenclature of morphological terms is used according to Beckmann *et al.* (2015) and Mayer (2016).

Synchrotron radiation-based X-ray micro-computed tomography

For synchrotron radiation-based X-ray micro-computed tomography (SR-µCT), specimens or containers with specimens were glued onto standardized sample holders (HZG, Geesthacht, Germany) using superglue (Pattex, Henkel AG & Co. KGaA, Düsseldorf, Germany). All SR-µCT analyses were conducted at the beamline P05 of the storage ring PETRA III (Deutsches Elektronen-Synchrotron — DESY, Hamburg, Germany) operated by Helmholtz-Zentrum Geesthacht (Haibel *et al.*, 2010; Greving *et al.*, 2014). While one unstained specimen (in absolute ethanol) was measured using single grating differential phase-contrast (=DPC) setup as previously described (Hipp *et al.*, 2014; Wilde *et al.*, 2016), the remaining specimens were analysed using attenuation contrast (Greving *et al.*, 2014), herein referred to as standard SR-µCT setup. The photon energy applied varied between 8 and 23 keV according to the electron density of samples treated with distinct contrasting methods (Table 1). A total of 900

radiograms were recorded at equal steps between 0 and π. The tomographic reconstruction algorithm "back-projection of filtered projections" (Huesman *et al.*, 1977) was used to yield 32-bit floating image stacks with isotropic voxel size of 2.47 µm.

Qualitative image analyses

For qualitative image analyses, original 32-bit float data were scaled to smaller 8-bit datasets. Image stacks were cropped and subtracted from a previously generated, semi-automatic binary mask to remove the surrounding background and to improve the dataset handling. The visual evaluation of each contrasting method was carried out using the open-source software package Fiji (Schindelin *et al.*, 2012) by comparing corresponding regions across the image stacks. 3D volume rendering showing the virtual anatomical planes used in our study (Fig. 1B) was performed in Amira 6.0.1 (FEI Visualization Sciences Group, Burlington, MA, USA). Final panels were designed with Illustrator CS5 (Adobe Systems, San José, California, USA) and exported in the Tagged Image File Format.

Quantitative image analyses

Quantitative analyses were based on original 32-bit float image stacks obtained from the reconstruction algorithm without further adjustments or scaling of grey values, which solely represented the attenuation coefficient µ for the given pixel volume. Image measurements were performed in Fiji. For optimal visualisation, the window/level function was initially utilized in order to adjust brightness and contrast while preserving the original grey value of each pixel without applying the chosen settings. For comparative analyses, four internal organs and their associated structures were selected, including the brain (neuropil and perikaryal layer), the jaw (sclerotized and soft parts), the eye (cornea, lens [=vitreous body], photoreceptor cell layer, and visual neuropil), and the pharynx (pharyngeal musculature). Grey value distribution within each of these internal structures was inferred by manually

selected areas with similar sizes in corresponding regions of the same tissue using the freehand selection tool within each specimen. The obtained measurements (including area, frequency, mean value, median, standard deviation, and minimum and maximum grey values) were exported to Excel 2010 (Microsoft Corporation, Redmond, Washington, USA) for quantitative analyses. For comparison, the obtained series of measurements were normalized by dividing each value of the series by the highest value of the entire series. In addition, boxplots were generated for all individual tissue types selected, containing the entire measurement series for each dataset using MATLAB (MathWorks®, Inc., Natick, Massachusetts, USA). Tissue-specific signal-to-noise ratios were calculated for each contrasting approach by dividing the average grey value of the selected tissue type by the grey value standard deviation extracted from the surrounding background, based on the formula ($SNR = \mu_{signal}/\delta_{background}$). The surrounding background (δ) corresponds to grey values of the medium, in which each specimen was scanned, i.e., either air, ethanol, or epoxy resin. Mean grey value signal (μ) was measured by choosing specific regions of target tissues.

Results

SR-µCT analyses of *E. rowelli* revealed that specimens treated with different stains (Table 1) exhibit distinct visualisation properties for both soft tissues and sclerotized structures. Comparative analyses of virtual sections through corresponding body regions of these specimens (Fig. 1B) demonstrate major differences in contrast, level of imaging detail, and image noise within and between organs and tissues, including the brain, eyes, jaws, and musculature (Figs. 2–5). The body cavity appears darker than the surrounding tissues and organs in all datasets. The greatest difference in grey values between body cavity and tissues/organs is observed in the OsO_4-stained, critical point dried specimen (Figs. 2E; 3E), whereas the lowest variation occurs in the specimen treated with OsO_4 and embedded in Araldite® (Figs. 2F; 3F). The latter exhibits the brightest body cavity and the lowest contrast

within the tissues (Figs. 2F; 3F). Nevertheless, the overall contrast in this specimen is homogenous and details of tissues and structures are recognizable. On the contrary, the specimen treated with iodine also shows a bright body cavity and low contrast within tissues, but does not allow unambiguous identification of internal structures (Figs. 2H; 3H).

The specimens treated with OsO_4 vapour and ruthenium red (Figs. 2B,D; 3B,D) as well as unstained specimens analysed using standard and DPC SR-µCT setups (Figs. 2A,G; 3A,G) exhibit comparable visualisation of tissues and structures, even though the unstained specimen imaged using DPC shows comparatively higher contrast between tissues and structures. Notably, the specimen stained with OsO_4 vapour exhibits well-defined peripheral structures, including dermal papillae, body wall musculature and the mouth region, which are brighter than tissues and organs located further internally (Figs. 2B, 3B). Consequently, a bright-to-dark gradient is observed in different regions of this specimen, for example, along the dorsoventral axis of the brain (Fig. 2B). Finally, the PTA stain revealed strong differences in contrast between tissues and organs (Figs. 2C; 3C) but also retrieved prominent dark areas within the innermost structures, such as inside the brain and within the pharynx (Figs. 2C; 3C).

The eight approaches tested also resulted in different levels of image noise, especially evident within the body cavity. The unstained specimen analysed using the standard SR-µCT setup and the specimen treated with ruthenium red exhibit the most prominent image noise among the datasets (Figs. 2A,D; 3A,D), followed respectively by specimens stained with OsO_4 vapour and PTA stain (Figs. 2B,C; 3B,C). Image noise is less evident in specimens treated with OsO_4 and either critical point dried or embedded in Araldite®, in which the body cavity appears nearly black (Figs. 2E; 3E) or shows similar grey values to the surrounding tissues and organs (Figs. 2F; 3F), respectively.

Visualisation of neural tissues

The onychophoran brain consists of an outer perikaryal layer, which contains the neuronal cell bodies that surround a complex neuropil structure (Mayer, 2016), both of which can be distinguished from each other in most techniques applied (Figs. 2A–G; 3A–G). The only exception is observed in the specimen treated with iodine, which does not show any difference in grey values between the neuropil and the perikaryal layer within the brain (Figs. 2H; 3H). Delimitation between the perikaryal layer and the neuropil can be established by different means, depending on the approach or staining agent used. In general, differences in grey values are observable between these brain areas, with the neuropils appearing darker than the perikaryal layer. This is observed in unstained specimens (Figs. 2A,G; 3A,G) as well as in those treated with OsO_4 vapour (Figs. 2B; 3B), PTA (Figs. 2C; 3C) and ruthenium red (Figs. 2D; 3D). However, the border between the neuropils and perikaryal layer is less distinct in the specimen stained with OsO_4 vapour, given the similar grey values among them and the overall dark appearance of the brain (Figs. 2B; 3B). On the other hand, the neuropil region appears similar or even slightly brighter than the perikaryal layer in specimens stained with OsO_4 and either critical point dried (Figs. 2E; 3E) or embedded in Araldite® (Figs. 2F; 3F). Nevertheless, the brain neuropil and perikaryal layer are recognizable by their different textures in these specimens — the neuropils appear smooth, whereas the perikaryal layer shows a granulated appearance (Figs. 2E,F; 3E,F). Separate analyses of the brain neuropil and the perikaryal layer revealed only minor variation in grey values within each of these areas in all datasets.

Visualisation of musculature

The onychophoran musculature is revealed at different levels of contrast and detail depending on the approach used, represented here by the pharynx — a prominent structure mainly composed of muscle tissue (Fig. 4A–H). In general, approaches using OsO_4 as staining agent as well as the unstained specimen analysed using DPC generate a homogenous grey value

distribution within this tissue type (Fig. 4B,E–G), whereas the unstained specimen analysed with the standard SR-µCT setup and those treated with PTA and ruthenium red show a heterogeneous, granulated musculature (Fig. 4A,C,D). Moreover, the muscle tissue is comparatively brighter in the specimen analysed using DPC (Fig. 4G) and those stained with OsO_4 and either critical point dried or embedded in resin (Fig. 4E,F). On the other hand, the musculature is generally darker in the remaining samples (Fig. 4A–D).

Individual bundles of muscle fibres are only distinguishable in the unstained specimen analysed with the standard SR-µCT setup (Fig. 4A) and in that stained with PTA (Fig. 4C), whereas the remaining approaches do not allow a clear distinction between sets of muscle fibres. The cuticular lining of the pharyngeal lumen is revealed as a thin, bright line in nearly all samples (Fig. 4A–E,G), except for the specimen embedded in Araldite®, in which this layer is indistinct (Fig. 4F). Unfortunately, the characteristics of the pharynx and its muscular tissue are indistinct in the specimen treated with iodine (Fig. 4H), thus not allowing a comparison with the other methods used.

Visualisation of optic structures

We observed a remarkable variation in the level of contrast and detail of optic structures depending on the contrasting technique applied (Fig. 5A–H). The cornea, which constitutes the outer structure of the eye, is recognizable as a thin layer in all methods tested, except for the specimen treated with OsO_4 and subsequently embedded in Araldite®, in which this structure is indistinguishable from the lens (Fig. 5F). The lens appears in all specimens as a roundish structure situated beneath the cornea. In the unstained specimen analysed with the standard SR-µCT setup (Fig. 5A) as well as in those treated with OsO_4 vapour (Fig. 5B) and PTA (Fig. 5C), the lens exhibits a gradient of grey values from a brighter outer surface to a darker centre. This gradient is less evident in specimens treated with ruthenium red (Fig. 5D) and OsO_4 followed by critical point drying (Fig. 5E), and is completely undetectable in the

remaining samples, including the OsO_4-stained, Araldite®-embedded specimen (Fig. 5F), the unstained specimens analysed using the DPC setup (Fig. 5G), and the specimen treated with iodine (Fig. 5H).

Underneath the lens, the photoreceptor cell layer of the retina is subdivided into an outer rhabdomeric region, a thin pigment layer, and a perikaryal layer of photoreceptors (Mayer, 2006b; Beckmann *et al.*, 2015). The rhabdomeric region is located immediately below the lens and is identifiable in all specimens analysed (Fig. 5A–H). Moreover, the distribution of grey values within the rhabdomeric region is nearly homogenous in these specimens, except for the unstained dried (Fig. 5A) and the ruthenium red stained (Fig. 5D) specimens, in which this region rather shows a strongly granulated appearance.

The pigment layer is evidenced as a thin, c-shaped line surrounding the basis of the rhabdomeric region. It appears brighter than the rhabdomeric region and the perikaryal layer of photoreceptors in most techniques applied (Fig. 5B,D–H), but shows similar grey values and is hardly recognizable from adjacent tissues in the unstained specimen analysed with the standard SR-µCT setup (Fig. 5A) and PTA-treated (Fig. 5C) specimens. Finally, the pigment layer is followed by the perikaryal layer of photoreceptors and the visual neuropil. These two regions appear similar to each other and show just minor grey value differences in most staining techniques tested (Fig. 5A–F), being only completely indistinguishable in the unstained specimen analysed by DPC or in that treated with iodine (Fig. 5G,H). Similar to the rhabdomeric region, these two areas show a homogenous distribution of grey values in most specimens but appear granulated in the unstained specimen analysed with the standard SR-µCT setup (Fig. 5A) and the ruthenium red stained specimens (Fig. 5D). Furthermore, the visual neuropil is darker than the perikaryal layer in the unstained specimen analysed with the standard SR-µCT setup (Fig. 5A) as well as in the specimen treated with PTA (Fig. 5C), whereas these structures exhibit similar contrast in the remaining specimens and are only distinguishable from each other by their different texture.

Visualisation of sclerotized structures

In all techniques tested, the outer sclerotized, cuticular parts of the onychophoran jaw blades appear brighter than the internal soft tissue and associated musculature (Fig. 2A-H). This difference in grey values is, however, most prominent in the unstained specimen analysed using DPC (Fig. 2G) as well as in the specimens treated with ruthenium red (Fig. 2D) and iodine (Fig. 2H), in which the sclerotized parts of the jaws appear as a well-defined bright area surrounding the soft tissue. The smallest difference between sclerotized structures and soft tissues associated with the jaw is observed in the OsO_4-stained, Araldite®-embedded specimen, given the accentuated brightness of all tissue types in this sample (Fig. 2F). The soft tissue associated with the jaw is nearly homogenous in specimens treated with OsO_4 vapour, PTA, iodine, and OsO_4 followed by either critical point drying or Araldite® embedding (Figs. 2B,C,E,F,H), whereas it appears heterogeneous in both unstained specimens and the sample treated with ruthenium red (Fig. 2A,D,G).

Quantitative analyses of SR-µCT datasets

Grey value measurements obtained from selected tissue types revealed that these regions exhibit a characteristic distribution of grey values in each method applied (Fig. 6). This is clearly demonstrated by the different ranges of their corresponding plots along the y-axis. The widest range of grey values (including the minimum and the maximum) is observed in the visual neuropil of the specimens treated with ruthenium red, while the narrowest range is found in the brain neuropil of the unstained specimen analysed using DPC.

Our data further show that the distribution of scattered grey values within a structure as well as of predominant grey values (mean + H-spread values) also varies substantially among the datasets. In general, the scattered grey values range from a narrow distribution in the OsO_4-stained, Araldite®-embedded specimen, to a wide distribution in the specimen

treated with PTA (Fig. 6). The distribution of predominant grey values (blue boxes in Fig. 6), however, is comparatively wide in the specimen treated with ruthenium red and remarkably narrow in the unstained specimen analysed using DPC (except for the sclerotized parts of the jaw; Fig. 6). Moreover, the distribution of predominant grey values overlaps at different degrees among structures of a single specimen. This overlap is most prominent in the specimen treated with iodine as well as in the unstained specimen analysed using DPC, in which nearly all structures show grey values distributed within a very limited range (0.1–0.3). Exceptions include the eye lens and the sclerotized parts of the jaw, which in these two specimens show predominant grey values between 0.5 and 0.8 (Fig. 6). On the other hand, the OsO_4-stained, Araldite®-embedded specimen exhibits the smallest overlap of predominant grey values among structures (Fig. 6). Nevertheless, the overlap of grey values becomes substantially more prominent in all datasets, if the total range between minimum and maximum values is taken into account instead.

Differences between the approaches tested are also observed in quantitative analyses using tissue-specific signal-to-noise ratio (=SNR; Table 2). Within the total SNR range from 10 dB to 89 dB, the unstained specimen analysed using DPC displays the highest values among all approaches (51–89 dB), whereas SNR measurements obtained from the unstained dried (10–33 dB), OsO_4 vapour-treated (19–26 dB) and RR stained specimen (12–32 dB) possess among the lowest levels. Samples treated with PTA (24–44 dB), OsO_4 (32–54 dB), OsO_4 embedded (30–62 dB) and iodine embedded (31–73 dB) show intermediate SNR values.

Discussion

Previous comparative studies aiming to optimize CT imaging of zoological samples have mainly been focused on animals with hard tissues, such as vertebrates and arthropods

(Metscher, 2009a, b; Pauwels *et al.*, 2013; Sombke *et al.*, 2015; Swart *et al.*, 2016), while suitable approaches for soft-bodied invertebrates remain largely understudied. Herein, we used SRμCT to assess the benefits and disadvantages of different staining approaches to the CT imaging of Onychophora — a small group of soft-bodied invertebrates crucial for investigating, for example, the evolutionary origin and diversification of arthropods (spiders, millipedes, crustaceans, insects, etc.). Our data revealed that selecting the contrasting method and imaging setup is a vital step for proper visualisation of different soft tissues in Onychophora, as the level of imaging detail varies substantially among structures depending on the method used. For example, the visualisation of sclerotized and optic structures varied from highly evident to nearly indistinguishable from the surrounding tissue in our datasets. Given this extreme variation, it is difficult to suggest a standard contrasting approach that would allow optimal visualisation of all structures simultaneously. Instead, the most suitable imaging approach will largely depend on the structure of interest.

According to our findings, the best overall staining for Onychophora is achieved by using a 2% OsO_4 solution. Osmium tetroxide has long been used as a fixative and staining agent for transmission electron microscopy (=TEM), known for its property of binding lipids and proteins (Angermüller & Fahimi, 1982). The specimen stained herein with 2% OsO_4 and critical point dried allowed for the best distinction of internal structures in 2D visualisation. On the other hand, it revealed only few details within individual tissues and organs as compared to other approaches tested.

A similar effect was observed in the specimen treated with 2% OsO_4 and embedded in Araldite®. However, this specimen showed a lower visual contrast among structures than the OsO_4-stained, critical point dried specimen. The loss of contrast associated with the embedding process makes it more difficult to distinguish structures from background and body cavities, thus complicating subsequent image processing steps. Nevertheless, embedding the specimen in Araldite® has two advantages: (i) it stabilizes the sample, which helps to

decrease potential movement artefacts during imaging; and (ii) the same specimen can be used for further morphological analyses, such as semi-thin or ultra-thin sectioning for light and transmission electron microscopy, respectively (Handschuh *et al.*, 2013; Sengle *et al.*, 2013; Morales *et al.*, 2016).

The remaining contrasting approaches tested did not retrieve optimal overall contrast but still proved to be useful for imaging specific onychophoran structures or tissue types. With respect to the nervous system, PTA provided the highest contrast differences between the neuropil and the perikaryal layer. PTA has been used in histology methods because of its property to stain connective tissue fibres (e.g., fibrin, collagen and other components of connective tissue; Quintarelli *et al.*, 1971), which are abundant in the nervous tissue. However, this method also revealed dark areas inside the brain, which do not correspond to any morphological structure and most likely represent a staining artefact. This may have occurred either because the PTA concentration was too low, or because PTA requires a longer incubation time for penetrating the whole sample, or both. Metscher (2009b) pointed out that PTA requires long incubation times because of the large size of its molecules and proposed incubation periods of overnight or longer for this staining agent. Accordingly, we used a 5-day incubation for our sample, considering its size and the slow penetration of PTA. A recent study demonstrated, however, that staining with PTA requires even longer incubation periods (~7 days or longer) to retrieve satisfactory results (Swart *et al.*, 2016). Unfortunately, this study only became available after we conducted our experiments and we were unable to repeat them given the limited number of samples available and time constraints at the SR-µCT facilities. The results presented by Swart *et al.* (2016) suggest, therefore, that the PTA protocol used in the present study can still be further optimised for onychophorans, even though it is difficult to assert at the current stage whether or not longer incubation times would indeed produce better results. Therefore, this is an issue to be tested in future studies.

Nevertheless, our results show that ruthenium red might be a suitable alternative to PTA for studying nervous tissue in Onychophora. Ruthenium red also provided acceptable contrast of this tissue and allowed for clear differentiation between neuropil and perikaryal layer. Different from PTA, ruthenium red mainly stains mucopolysaccharides, but also interacts with ion channels, which are abundant in the nervous system (Luft, 1971). Since ruthenium red apparently does not show the penetration issues observed for PTA, we consider it one of the most suitable staining agents for the onychophoran nervous system.

We also tested an approach that used OsO_4 vapour for both fixing and staining the specimen, as OsO_4 is highly volatile (Griffith, 1965 *apud* Griffith, 1974). Similar to PTA, this method seems to exhibit limited tissue penetration. Consequently, only structures located close to the external surface of the animal, such as the transverse musculature, appeared conspicuously stained but the overall contrast decreased gradually towards the interior of the body. On the other hand, this method allowed the best visualisation of optic structures that comprise the onychophoran eye. We believe that the low penetration of OsO_4 vapour may be associated with the short exposure time of the specimen to the vapour. Additionally, it is also reasonable to assume that the penetration speed of OsO_4 may be associated with its concentration, which is considerably lower in the vapour than in solution. Nevertheless, longer exposure times are undesirable in our case, because onychophorans dry out quickly after death and exposing the specimen to OsO_4 vapour for longer periods would thus introduce deformation and shrinkage artefacts. Therefore, this method can only be recommended if one aims to study the morphological features associated with the external-most tissues of onychophorans.

Finally, our staining with iodine retrieved the most unexpected results among our datasets. Iodine has been successfully applied in many CT studies of diverse vertebrates and arthropods (Metscher, 2009b; Pauwels *et al.*, 2013; Gignac & Kley, 2014; Sombke *et al.*, 2015; Gignac *et al.*, 2016, Swart et al. 2016). Similar satisfactory results were expected

herein, given the property of iodine to interact with a wide range of molecules such as amino acids, nucleotides and fatty acids (Gignac & Kley, 2014), thus providing, in theory, a good overall staining of tissues and organs. Three putative facts may account for the suboptimal results obtained herein for this staining method: either (1) the incubation time was not sufficient, (2) iodine staining is incompatible with the Araldite® embedding protocol, or less likely, (3) iodine could cross-react with the fixative used. The reported duration of incubation for iodine staining ranges from overnight up to ten days for invertebrates (cephalopods, myriapods, polychaetes, hexapods) and from seven hours up to several weeks for vertebrates (amphibians, reptiles, birds, mammals), as summarized by Gignac *et al.* (2016). Our samples were incubated overnight in iodine, i.e., the minimum time described for an invertebrate, hence longer staining times could indeed yield better results.

A putative connection between fixative and staining agent has previously been suggested (Sombke *et al.*, 2015), raising the question of whether or not our suboptimal results arose from the previous specimen fixation with glutaraldehyde. However, satisfactory images of iodine-stained specimens fixed with glutaraldehyde (with or without formalin) have already been shown in the literature (Metscher, 2009a, b). Furthermore, Metscher (2009a) tested different fixation/staining methods and concluded that, despite a putative connection between fixative and staining agent, all stains can be successfully used after any common fixation method. Therefore, we believe that in our case the interaction between staining agent and fixative is possible but unlikely to be the source of the suboptimal results. We also rule out the possibility that an insufficient number of washing steps was a putative reason for the unsatisfactory imaging quality obtained, as samples can theoretically be scanned in actual iodine staining solution and still retrieve reasonable results.

Finally, we believe that the low contrast observed in this specimen is most likely associated with the embedding process of the iodine sample in Araldite®. Iodine is known to be very stable in 100% ethanol, but it is unclear whether this stability is affected when the

sample is transferred to 100% acetone, a transitional solvent used for embedding the sample in Araldite®. Neither is it known whether or not iodine reacts with the resin itself, since unpolymerized resins also act as solvents (Dykstra & Reuss, 2003). As observed for OsO_4, the sample embedded in Araldite® shows substantially weaker contrast than the one that was dried. Therefore, it is possible that iodine staining is not a suitable approach for onychophoran samples that are to be subsequently embedded and scanned in resin.

In addition to approaches involving staining agents, we also performed SR-µCT experiments using unstained specimens. The motivation behind imaging unstained specimens arose from the fact that a great number of onychophoran species was described in the late 19th and early 20th centuries (Oliveira *et al.*, 2012) and their type specimens were placed in scientific collections at museums and research institutions worldwide. Today, many of these species are still only known from their type material, as they were collected in areas where big cities developed and may thus no longer exist in nature. This type material therefore becomes the only source of information for these species, but is generally unavailable for any analyses that would affect, change or destroy the specimen. Fortunately, our findings are in line with previous studies of museum material (Ziegler, 2012; Fernández *et al.*, 2014) and show that a substantial amount of information can still be gleaned from unstained onychophoran specimens, irrespective of whether they are found in dry or wet conditions.

The ability to visually distinguish between structures in our datasets, however, does not necessarily mean that these structures can be easily separated from each other using software tools. This is because the digital segmentation of complex biological systems, such as the structures studied herein, commonly rely on a preliminary automatic or semi-automatic distinction of structures based on their specific grey values, which ideally should not overlap (Pham *et al.*, 2000). An aspect commonly influencing morphological segmentation is the appearance of image noise, which was herein quantified using signal-to-noise ratio (=SNR) measurements obtained by extracting from the informative data (signal) and the standard

derivation of image noise from the surrounding medium (herein air, ethanol, or epoxy resin). In this case, the higher the standard derivation values, the more image noise and consequently the lower the SNR values, whereas high SNR values mean a clearer differentiation between image signal and image noise.

Our data suggest, however, that other factors such as resolution and contrast may have higher influence on the detectability of structures than lower level of image noise in the analysed data sets. Considering solely the SNR values (Table 2), for example, one may assume that the best approach for morphological segmentation in Onychophora would be analysing either unstained specimens using a DPC setup or, for standard setup, samples treated with OsO_4 (dried or embedded) and/or iodine. Samples treated with PTA, OsO_4 vapour, ruthenium red and/or unstained would rather produce comparatively suboptimal results (Table 2). However, this scenario does not entirely reflect the results of additional quantitative and qualitative analyses presented herein, as it is clearly the case for the sample contrasted with iodine. This approach retrieved unsatisfactory results in qualitative as well as in box-and-whisker plots but still shows high SNR values. The latter most likely represent a methodological artefact arising from a low standard derivation for image noise, especially in high absorptive regions such as in the onychophoran jaws and eyes.

It should also be mentioned that different scan media have different attenuation coefficients and lead to different signal intensities and SNR values. Consequently, the SNR measurements presented herein are only partly comparable to each other. Yet, these measurements demonstrate tendencies in SNR values and may also provide useful information on which tissue shows reasonable contrast difference to the background noise, considering that the contrasting method and the scan medium are taken into account. Since high SNR values can arise from distinct tissue signal or alternatively from low image noise in the surrounding background, a synergy of different quantitative methods is important to evaluate the most suitable approach for specific purposes.

In this respect, we also measured grey value distribution in different structures of the onychophoran *E. rowelli* and used box-and-whisker plot analyses to infer how likely these morphological features can be automatically segmented in each of our datasets. Similar quantitative assessment and comparison of CT data has previously been presented for a vertebrate (chick embryos) and insects (Metscher, 2009a; Swart *et al.*, 2016), even though Metscher (2009a) only provided a simplified histogram comparing stains per method tested and Swart *et al.* (2016) rather analysed stain uptake rates for each tested staining reagent. Therefore, a direct comparison of our data with these studies is difficult, as none of them quantitatively compared the grey values among tissue types in different CT datasets.

In contrast to these previous studies (Metscher, 2009a; Swart *et al.*, 2016), we opted for box-and-whisker plot analyses over histogram graphics because the former method provides a good overview of how grey values are distributed within a single structure and, at the same time, how structures differ from each other in the same dataset, thus facilitating comparative analyses. Our findings show that the specific grey values of most onychophoran structures, which are visually distinct from each other, overlap substantially in quantitative analyses. This indicates that an automatic segmentation of these structures would be difficult in our datasets given their similar grey values, especially when the structures are topologically close to each other. In this case, a time-consuming manual segmentation of these structures would be required for reconstructing them three-dimensionally. Besides the segmentation using image intensities, one could consider applying other segmentation algorithms, which are based on the underlying texture characteristics of the tissue/structure. These tools are currently available for the free software ImageJ ("Trainable Weka Segmentation"; Arganda-Carreras *et al.*, 2017) or in the standalone software "ilastik" (Sommer *et al.*, 2011). Although our attempt to apply these algorithms to our onychophoran datasets was unsuccessful, we believe that reconstructions of morphological structures from µCT data sets will greatly benefit from further development of texture-based segmentation algorithms.

The grey value distribution of the structures analysed show different degrees of overlap, depending on the dataset chosen. For example, if we consider only the predominant grey values of each structure, an automatic segmentation would be very difficult in the unstained specimen analysed with DPC, as the grey values of most morphological structures lie within a very limited range in this specimen. On the other hand, this process would be easier to apply in the specimen stained with OsO_4 and embedded in Araldite®, given the distant grey values among structures with only little overlap. Our findings suggest that, among the eight approaches tested, staining with OsO_4 and either embedding the specimen in Araldite® or subjecting it to critical point drying is the preferable method for an automatic segmentation of internal features in Onychophora. Nevertheless, this method may be especially problematic for segmentation of substructures within a certain tissue, for example, the neuropils and the perikaryal layer of the onychophoran brain, thus leading to the conclusion that the most suitable CT approach for studying Onychophora will largely depend on the target tissue or structure.

Conclusion

In this study, we comparatively tested different protocols for SR-µCT studies of onychophorans. As demonstrated herein, this method is very promising for investigating several morphological aspects of these animals and, in combination with different staining agents and imaging approaches, allows target structures to be depicted at a high level of detail. According to our findings, 2% OsO_4 might be the best agent for general staining in onychophorans, as indicated by our qualitative and quantitative analyses. Moreover, the acceptable images obtained from unstained specimens suggest that a wealth of new data may be generated from understudied taxa of Onychophora, including rare species that lack recent records but have their type specimens placed in museums and scientific collections. On the other hand, our findings also show that issues like incubation times, penetration speed and

sample thickness, must be critically considered before proceeding with any CT experiments with Onychophora. Furthermore, analysing their soft tissues using CT techniques can be problematic, as contrasting and imaging approaches may retrieve substantial overlap of grey values among structures. Consequently, the automatic segmentation of many morphological structures in Onychophora becomes difficult and a manual segmentation remains the principal way to tell them apart. However, we believe that this situation may be improved in the near future, when specific markers similar to antibody staining used for fluorescent and confocal microscopy (e.g., Mayer & Whitington, 2009; Martin *et al.*, 2017b) or gold nanoparticle labelling used for transmission electron microscopy and nanomedicine (Mayhew *et al.*, 2009; Cole *et al.*, 2015) also become available for SR-µCT imaging. Meanwhile, the results presented herein may be helpful for onychophorologists who apply CT techniques in their research. Whether or not the protocols tested herein would produce similar results in other groups of soft-bodied invertebrates remains to be tested.

Acknowledgements

We thank David M. Rowell, Noel N. Tait and Paul Sunnucks for their help with permits over the years. Noel N. Tait, Dave M. Rowell, Paul Sunnucks, Franziska A. Franke, Sandra Treffkorn and Michael Gerth are kindly acknowledged for helping during specimen collection. We are grateful to members of the Mayer laboratory for their help with animal cultures. Three anonymous reviewers are acknowledged for their valuable comments on the manuscript. This study was supported by grants from the Deutsches Elektronen-Synchrotron (DESY: I-20150213) to JUH and GM, Conselho Nacional de Desenvolvimento Científico e Tecnológico (CNPq Brazil: 290029/2010-4) and the Zentrale Forschungsförderung of the University of Kassel (ZFF: 1970/2016) to IdSO, the German Research Foundation (DFG: Ma 4147/3-1) to GM, and a German Academic Exchange Service (DAAD) scholarship to VG.

References

Angermüller, S. & Fahimi, H. D. (1982). Imidazole-buffered osmium tetroxide: an excellent stain for visualization of lipids in transmission electron microscopy. *Histochem. J.* **14,** 823–835.

Arganda-Carreras, I., Kaynig, V., Rueden, C., Eliceiri, K. W., Schindelin, J., Cardona, A. & Sebastian Seung, H. (2017). Trainable Weka Segmentation: a machine learning tool for microscopy pixel classification. *Bioinformatics* **33,** 2424–2426.

Baer, A. & Mayer, G. (2012). Comparative anatomy of slime glands in Onychophora (velvet worms). *J. Morphol.* **273,** 1079–1088.

Beckmann, H., Hering, L., Henze, M. J., Kelber, A., Stevenson, P. A. & Mayer, G. (2015). Spectral sensitivity in Onychophora (velvet worms) revealed by electroretinograms, phototactic behaviour and opsin gene expression. *J. Exp. Biol.* **218,** 915–922.

Blanke, A., Koch, M., Wipfler, B., Wilde, F. & Misof, B. (2014). Head morphology of *Tricholepidion gertschi* indicates monophyletic Zygentoma. *Front. Zool.* **11,** 16.

Cole, L. E., Ross, R. D., Tilley, J. M., Vargo-Gogola, T. & Roeder, R. K. (2015). Gold nanoparticles as contrast agents in x-ray imaging and computed tomography. *Nanomedicine* **10,** 321–341.

Dierick, M., Van Loo, D., Masschaele, B., Van den Bulcke, J., Van Acker, J., Cnudde, V. & Van Hoorebeke, L. (2014). Recent micro-CT scanner developments at UGCT. *Nucl. Instrum. Methods* **324,** 35–40.

Dykstra, M. & Reuss, L. (2003). *Biological Electron Microscopy: Theory, Techniques, and Troubleshooting*. 2nd Edition, Springer Science+Buisness Media, North Carolina State University, p. 534.

Falcone, R., Jacobsen, C., Kirz, J., Marchesini, S., Shapiro, D. & Spence, J. (2011). New directions in X-ray microscopy. *Contemp. Phys.* **52,** 293–318.

Fernández, R., Kvist, S., Lenihan, J., Giribet, G. & Ziegler, A. (2014). Sine systemate chaos? A versatile tool for earthworm taxonomy: non-destructive imaging of freshly fixed and museum specimens using micro-computed tomography. *PLOS ONE* **9,** e96617.

Friedrich, F., Pohl, H., Beckmann, F. & Beutel, R. G. (2013). The head of *Merope tuber* (Meropeidae) and the phylogeny of Mecoptera (Hexapoda). *Arthropod Struct. Dev.* **42,** 69–88.

Gignac, P. M. & Kley, N. J. (2014). Iodine-enhanced micro-CT imaging: methodological refinements for the study of the soft-tissue anatomy of post-embryonic vertebrates. *J. Exp. Zool. Part B* **322,** 166–176.

Gignac, P. M., Kley, N. J., Clarke, J. A., Colbert, M. W., Morhardt, A. C., Cerio, D., Cost, I. N., Cox, P. G., Daza, J. D., Early, C. M., Echols, M. S., Henkelman, R. M., Herdina, A. N., Holliday, C. M., Li, Z., Mahlow, K., Merchant, S., Müller, J., Orsbon, C. P., Paluh, D. J., Thies, M. L., Tsai, H. P. & Witmer, L. M. (2016). Diffusible iodine-based contrast-enhanced computed tomography (diceCT): an emerging tool for rapid, high-resolution, 3-D imaging of metazoan soft tissues. *J. Anat.* **228,** 889–909.

Greving, I., Wilde, F., Ogurreck, M., Herzen, J., Hammel, J. U., Hipp, A., Friedrich, F., Lottermoser, L., Dose, T., Burmester, H., Müller, M. & Beckmann, F. (2014). P05 imaging beamline at PETRA III: first results. *Proc. SPIE* **9212,** 1–8.

Griffith, W. (1974). Osmium tetroxide and its applications. *Platin. Met. Rev.* **18,** 94–96.

Haibel, A., Beckmann, F., Dose, T., Herzen, J., Ogurreck, M., Müller, M. & Schreyer, A. (2010). Latest developments in microtomography and nanotomography at PETRA III. *Powder Diffr.* **25,** 161–164.

Hammel, J. U., Herzen, J., Beckmann, F. & Nickel, M. (2009). Sponge budding is a spatiotemporal morphological patterning process: insights from synchrotron radiation-based x-ray microtomography into the asexual reproduction of *Tethya wilhelma*. *Front. Zool.* **6,** 19.

Handschuh, S., Baeumler, N., Schwaha, T. & Ruthensteiner, B. (2013). A correlative approach for combining microCT, light and transmission electron microscopy in a single 3D scenario. *Front. Zool.* **10,** 1–16.

Hipp, A., Beckmann, F., Lytaev, P., Greving, I., Lottermoser, L., Dose, T., Kirchhof, R., Burmester, H., Schreyer, A. & Herzen, J. (2014). Grating-based x-ray phase-contrast imaging at PETRA III. *Proc. SPIE* **9212,** 921206.

Hounsfield, G. N. (1973). Computerized transverse axial scanning (tomography): Part I. Description of system. *Brit. J. Radiol.* **46,** 1016–1022.

Huesman, R. H., Gullberg, G. T., Greenberg, W. L. & Budinger, T. F. (1977). RECLBL library users manual-donner algorithms for reconstruction tomography. Lawrence Berkeley Laboratory, University of California, Berkeley, USA.

Kerbl, A., Handschuh, S., Nödl, M.-T., Metscher, B., Walzl, M. & Wanninger, A. (2013). Micro-CT in cephalopod research: Investigating the internal anatomy of a sepiolid squid using a non-destructive technique with special focus on the ganglionic system. *J. Exp. Mar. Biol. Ecol.* **447,** 140–148.

Kirz, J. & Jacobsen, C. (2009). The history and future of X-ray microscopy. *J. Phys. Conf. Ser.* **186,** 012001.

Luft, J. H. (1971). Ruthenium red and violet. II. Fine structural localization in animal tissues. *Anat. Rec.* **171,** 369–415.

Martin, C., Gross, V., Hering, L., Tepper, B., Jahn, H., de Sena Oliveira, I., Stevenson, P. A. & Mayer, G. (2017a). The nervous and visual systems of onychophorans and tardigrades: learning about arthropod evolution from their closest relatives. *J. Comp. Physiol. A* **203,** 565–590.

Martin, C., Gross, V., Pflüger, H.-J., Stevenson, P. A. & Mayer, G. (2017b). Assessing segmental versus non-segmental features in the ventral nervous system of onychophorans (velvet worms). *BMC Evol. Biol.* **17,** 3.

Mayer, G. & Whitington, P. M. (2009). Neural development in Onychophora (velvet worms) suggests a step-wise evolution of segmentation in the nervous system of Panarthropoda. *Dev. Biol.* **335,** 263–275.

Mayer, G. (2006a). Origin and differentiation of nephridia in the Onychophora provide no support for the Articulata. *Zoomorphology* **125,** 1–12.

Mayer, G. (2006b). Structure and development of the onychophoran eyes — what is the ancestral visual organ in arthropods? *Arthropod Struct. Dev.* **35,** 231–245.

Mayer, G. (2016). Onychophora. In: Schmidt-Rhaesa, A., Harzsch, S. & Purschke, G. (ed.) *Structure and Evolution of Invertebrate Nervous Systems.* Oxford University Press, Oxford, pp. 390–401.

Mayer, G., Franke, F. A., Treffkorn, S., Gross, V. & Oliveira, I. S. (2015a). Onychophora. In: Wanninger, A. (ed.) *Evolutionary Developmental Biology of Invertebrates 3: Ecdysozoa I: Non-tetraconata.* Springer, Berlin, pp. 53–98.

Mayer, G., Oliveira, I. S., Baer, A., Hammel, J. U., Gallant, J. & Hochberg, R. (2015b). Capture of prey, feeding, and functional anatomy of the jaws in velvet worms (Onychophora). *Integr. Comp. Biol.* **55,** 217–227.

Mayhew, T. M., Mühlfeld, C., Vanhecke, D. & Ochs, M. (2009). A review of recent methods for efficiently quantifying immunogold and other nanoparticles using TEM sections through cells, tissues and organs. *Ann. Anat.* **191,** 153–170.

Metscher, B. D. (2009a). MicroCT for developmental biology: a versatile tool for high-contrast 3D imaging at histological resolutions. *Dev. Dyn.* **238,** 632–640.

Metscher, B. D. (2009b). MicroCT for comparative morphology: simple staining methods allow high-contrast 3D imaging of diverse non-mineralized animal tissues. *BMC Physiol.* **9,** 1–11.

Mizutani, R. & Suzuki, Y. (2012). X-ray microtomography in biology. *Micron* **43,** 104–115.

Morales, A. G., Stempinski, E. S., Xiao, X., Patel, A., Panna, A., Olivier, K. N., McShane, P. J., Robinson, C., George, A. J., Donahue, D. R., Chen, P. & Wen, H. (2016). Micro-CT scouting for transmission electron microscopy of human tissue specimens. *J. Microsc.* **263,** 113–117.

Müller, M., de Sena Oliveira, I., Allner, S., Ferstl, S., Bidola, P., Mechlem, K., Fehringer, A., Hehn, L., Dierolf, M., Achterhold, K., Gleich, B., Hammel, J. U., Jahn, H., Mayer, G. & Pfeiffer, F. (2017). Myoanatomy of the velvet worm leg revealed by laboratory-based nanofocus X-ray source tomography. *PNAS* **114,** 12378–12383.

Oliveira, I. S., Read, V. M. S. J. & Mayer, G. (2012). A world checklist of Onychophora (velvet worms), with notes on nomenclature and status of names. *ZooKeys* **211,** 1–70.

Pauwels, E., Van Loo, D., Cornillie, P., Brabant, L. & Van Hoorebeke, L. (2013). An exploratory study of contrast agents for soft tissue visualization by means of high resolution X-ray computed tomography imaging. *J. Microsc.* **250,** 21–31.

Pendar, H., Kenny, M. C. & Socha, J. J. (2015). Tracheal compression in pupae of the beetle *Zophobas morio*. *Biol. Lett.* **11**.

Pham, D. L., Xu, C. & Prince, J. L. (2000). Current methods in medical image segmentation. *Annu. Rev. Biomed. Eng.* **2,** 315–337.

Quintarelli, G., Zito, R. & Cifonelli, J. A. (1971). On phosphotungstic acid staining. I. *J. Histochem. Cytochem.* **19,** 641–647.

Schindelin, J., Arganda-Carreras, I., Frise, E., Kaynig, V., Longair, M., Pietzsch, T., Preibisch, S., Rueden, C., Saalfeld, S., Schmid, B., Tinevez, J.-Y., White, D. J., Hartenstein, V., Eliceiri, K., Tomancak, P. & Cardona, A. (2012). Fiji: an open-source platform for biological-image analysis. *Nat. Meth.* **9,** 676–682.

Sengle, G., Tufa, S. F., Sakai, L. Y., Zulliger, M. A. & Keene, D. R. (2013). A correlative method for imaging identical regions of samples by micro-CT, light microscopy, and electron microscopy: imaging adipose tissue in a model system. *J. Histochem. Cytochem.* **61,** 263–271.

Sombke, A., Lipke, E., Michalik, P., Uhl, G. & Harzsch, S. (2015). Potential and limitations of X-ray micro-computed tomography in arthropod neuroanatomy: a methodological and comparative survey. *J. Comp. Neurol.* **523,** 1281–1295.

Sommer, C., Straehle, C., Köthe, U. & Hamprecht, F. A. (2011). ilastik: interactive learning and segmentation toolkit. *Eighth IEEE International Symposium on Biomedical Imaging (ISBI)* Chicago, USA, 230–233.

Swart, P., Wicklein, M., Sykes, D., Ahmed, F. & Krapp, H. G. (2016). A quantitative comparison of micro-CT preparations in dipteran flies. *Sci. Rep.* **6,** 39380.

Weihmann, T., Kleinteich, T., Gorb, S. & Wipfler, B. (2015). Functional morphology of the mandibular apparatus in the cockroach *Periplaneta americana* (Blattodea, Blattidae) — a model species for omnivore insects. *Arthropod Syst. Phylo.* **73,** 477–488.

Wilde, F., Ogurreck, M., Greving, I., Hammel, J. U., Beckmann, F., Hipp, A., Lottermoser, L., Khokhriakov, I., Lytaev, P., Dose, T., Burmester, H., Müller, M. & Schreyer, A. (2016). Micro-CT at the imaging beamline P05 at PETRA III. *AIP Conf. Proc.* **1741,** 030035.

Ziegler, A. (2012). Broad application of non-invasive imaging techniques to echinoids and other echinoderm taxa. *Zoosymposia* **7,** 53–70.

Figure legends

Figure 1. The onychophoran *Euperipatoides rowelli*. Photograph of a living specimen (A) and volume rendering of SR-µCT data (B) showing the anterior body region and the virtual planes depicted in subsequent images of this work. an, antenna; hd, head; lg, leg; The specimen size in (A) is ~4 cm and in (B) ~2 cm.

Figure 2. Comparative imaging of the onychophoran head using different contrasting approaches. 2D visualisation of corresponding virtual cross sections through the head of *Euperipatoides rowelli*. Dorsal is up in all images. (A) Unstained specimen analysed using the standard SR-µCT setup. (B) Specimen treated with OsO_4 vapour. (C) Specimen treated with PTA (phosphotungstic acid). (D) Specimen treated with ruthenium red (RR). (E) Specimen treated with OsO_4 followed by critical point drying. (F) Specimen treated with OsO_4 followed by Araldite® embedding. (G) Unstained specimen analysed using DPC (differential phase-contrast). (H) Specimen treated with iodine followed by Araldite® embedding. br, brain (arrowhead, perikaryal layer; asterisk, neuropil); ey, eye; jw, jaw; scale bars: 200 µm.

Figure 3. Comparative imaging of the onychophoran head using different contrasting approaches. 2D visualisation of corresponding virtual horizontal sections through the head of *Euperipatoides rowelli*. Anterior is left in all images. (A) Unstained specimen analysed using the standard SR-µCT setup. (B) Specimen treated with OsO_4 vapour. (C) Specimen treated with PTA (phosphotungstic acid). (D) Specimen treated with ruthenium red (RR). (E) Specimen treated with OsO_4 followed by critical point drying. (F) Specimen treated with OsO_4 followed by Araldite® embedding. (G) Unstained specimen analysed using DPC (differential phase-contrast). (H) Specimen treated with iodine followed by Araldite® embedding. br, brain; ey, eye; ph, pharynx; scale bars: 200 µm.

Figure 4. Comparative imaging of the onychophoran pharynx using different contrasting approaches. 2D visualisation of corresponding virtual cross sections through the pharynx of *Euperipatoides rowelli*. Anterior is left in all images. (A) Unstained specimen analysed using the standard SR-µCT setup. (B) Specimen treated with OsO_4 vapour. (C) Specimen treated with PTA (phosphotungstic acid). (D) Specimen treated with ruthenium red (RR). (E) Specimen treated with OsO_4 followed by critical point drying. (F) Specimen treated with OsO_4 followed by Araldite® embedding. (G) Unstained specimen analysed using DPC (differential phase-contrast). (H) Specimen treated with iodine followed by Araldite® embedding. pl, pharyngeal lumen; pm, pharyngeal musculature; scale bars: 100 µm.

Figure 5. Comparative imaging of the onychophoran eye using different contrasting approaches. 2D visualisation of corresponding virtual cross sections through the optical structures of *Euperipatoides rowelli*. (A) Unstained specimen analysed using the standard SR-µCT setup. (B) Specimen treated with OsO_4 vapour. (C) Specimen treated with PTA (phosphotungstic acid). (D) Specimen treated with ruthenium red (RR). (E) Specimen treated with OsO_4 followed by critical point drying. (F) Specimen treated with OsO_4 followed by Araldite® embedding. (G) Unstained specimen analysed using DPC (differential phase-contrast). (H) Specimen treated with iodine followed by Araldite® embedding. Asterisks indicate the lens; dotted line demarcates the perikaryal layer of the photoreceptors; dashed line marks the visual neuropil. Note that the perikaryal layer of photoreceptors and the visual neuropil are indistinguishable in specimens scanned using DPC (G) or treated with iodine (H). co, cornea; pg, pigment layer; rh, rhabdomeric region; scale bars: 50 µm.

Figure 6. Quantitative comparison of grey value distribution within and among investigated organs in each dataset using box-and-whisker plots. Grey values of selected organs were

measured in each SR-μCT dataset and normalized to the entire measurement series. The plots show the minimum and maximum grey values (lower and upper horizontal black lines, respectively), the mean grey value (in red), the H-spread grey values (mean ±25%; blue box), and the scattered grey values above and below the H-spread values (whiskers; vertical black lines) for individual organs and tissues in each dataset. Zero represents black and 1.0 corresponds to white. Note that the organs with horizontally overlapping boxes require manual segmentation for 3D reconstruction. PTA, phosphotungstic acid; RR, ruthenium red.

Tables

Table 1. Preparation treatments and imaging parameters for the specimens scanned using SRμCT.

Fixation	N	Staining agent	Medium	CT setup	Magnification [factor]	Pixel size [μm]	Beam energy	Exposure time [ms]
paraformaldehyde	1	unstained	air	attenuation	9.7	2.46	8 keV	1850
glutaraldehyde	1	4% OsO_4 vapour	air	attenuation	9.7	2.46	8 keV	1850
paraformaldehyde	1	PTA	air	attenuation	9.7	2.46	23 keV	500
glutaraldehyde	1	ruthenium red	air	attenuation	9.7	2.46	8 keV	3100
glutaraldehyde	1	2% OsO_4	air	attenuation	9.7	2.46	22 keV	250
glutaraldehyde	1	2% OsO_4	embedded	attenuation	9.7	2.46	18 keV	200
glutaraldehyde	1	unstained	abs. ethanol	DPC	5	4.8	20 keV	200
glutaraldehyde	1	iodine	embedded	attenuation	9.2	2.60	15 keV	150

Table 2. Tissue-specific signal-to-noise ratio (SNR [dB]) for contrasting approaches analysed.

Sample	Eye lens	Rhabdomeric region	Visual neuropil	Jaw muscles	Sclerotized jaw parts	Pharynx	Neuropil layer	Perikaryal layer
Unstained	33	10	13	23	30	13	16	16
OsO_4 vapour	21	21	21	26	24	19	20	17
PTA	37	24	35	44	26	33	37	44
RR	26	12	14	22	32	19	18	21
OsO_4 solution	49	52	54	41	32	39	53	46
OsO_4 embedded	62	41	36	30	40	33	46	46
DPC	78	89	54	63	68	64	61	51
Iodine embedded	56	43	39	38	73	31	40	55

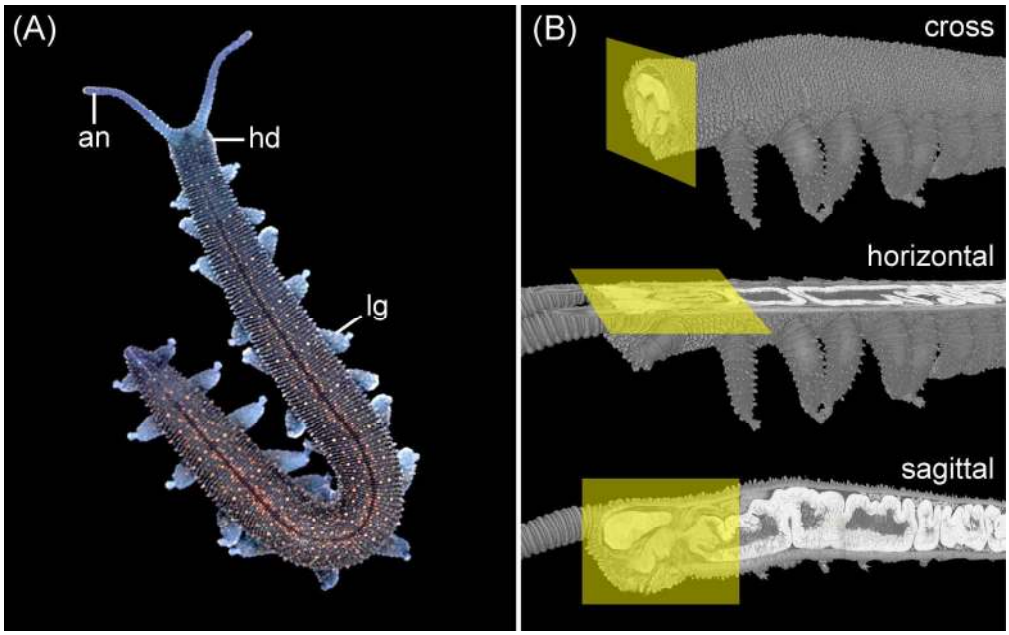

The onychophoran *Euperipatoides rowelli*.

167x105mm (300 x 300 DPI)

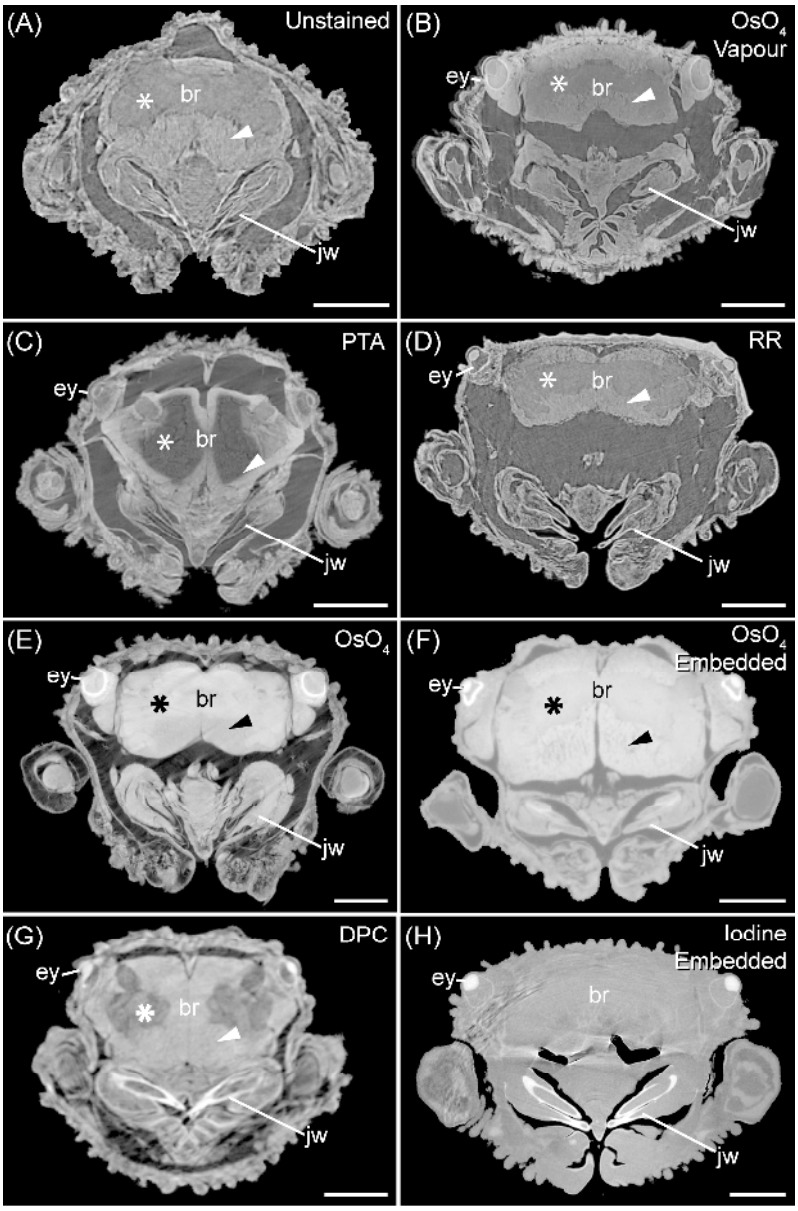

Comparative imaging of the onychophoran head using different contrasting approaches.

167x254mm (300 x 300 DPI)

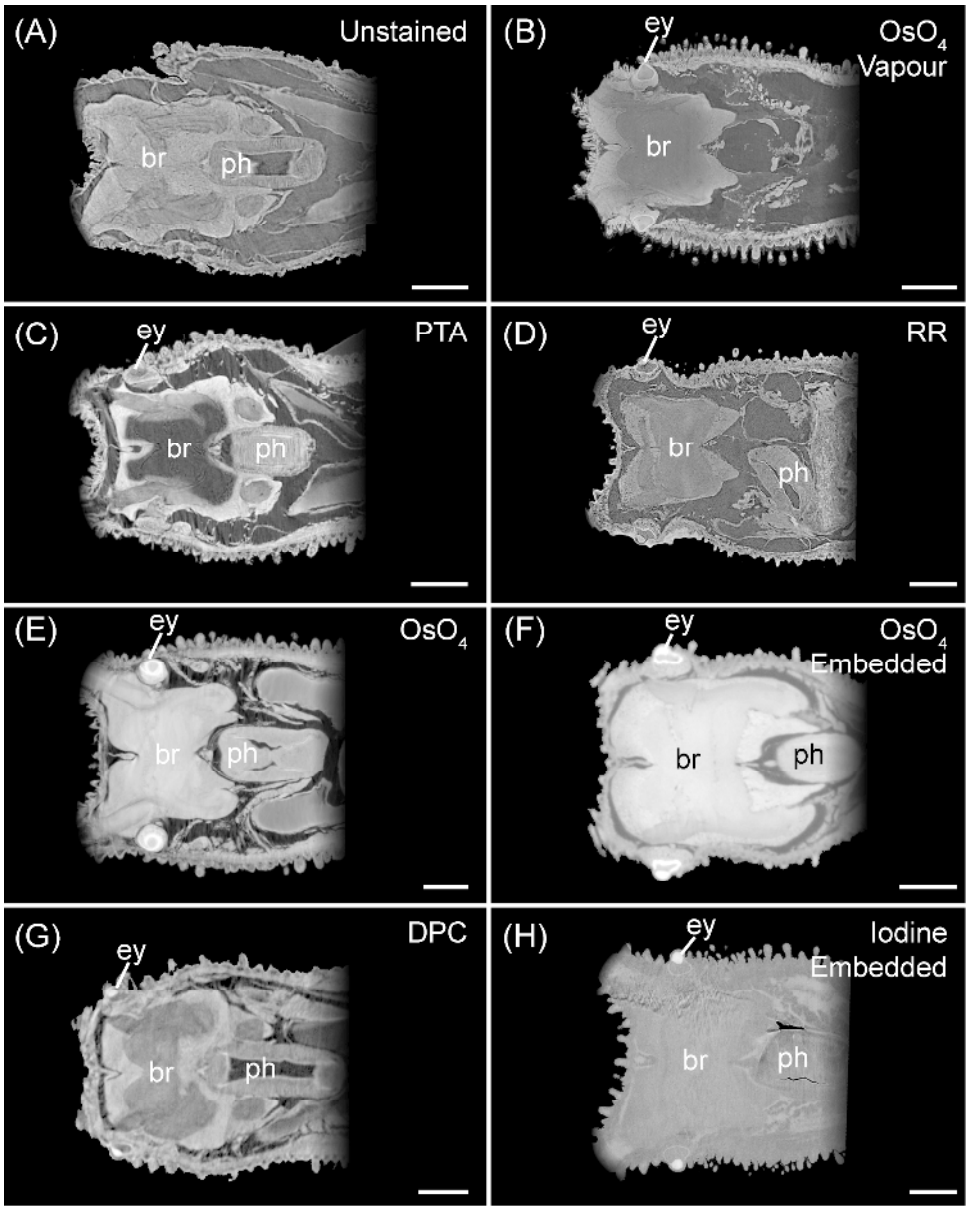

Comparative imaging of the onychophoran head using different contrasting approaches.

166x208mm (300 x 300 DPI)

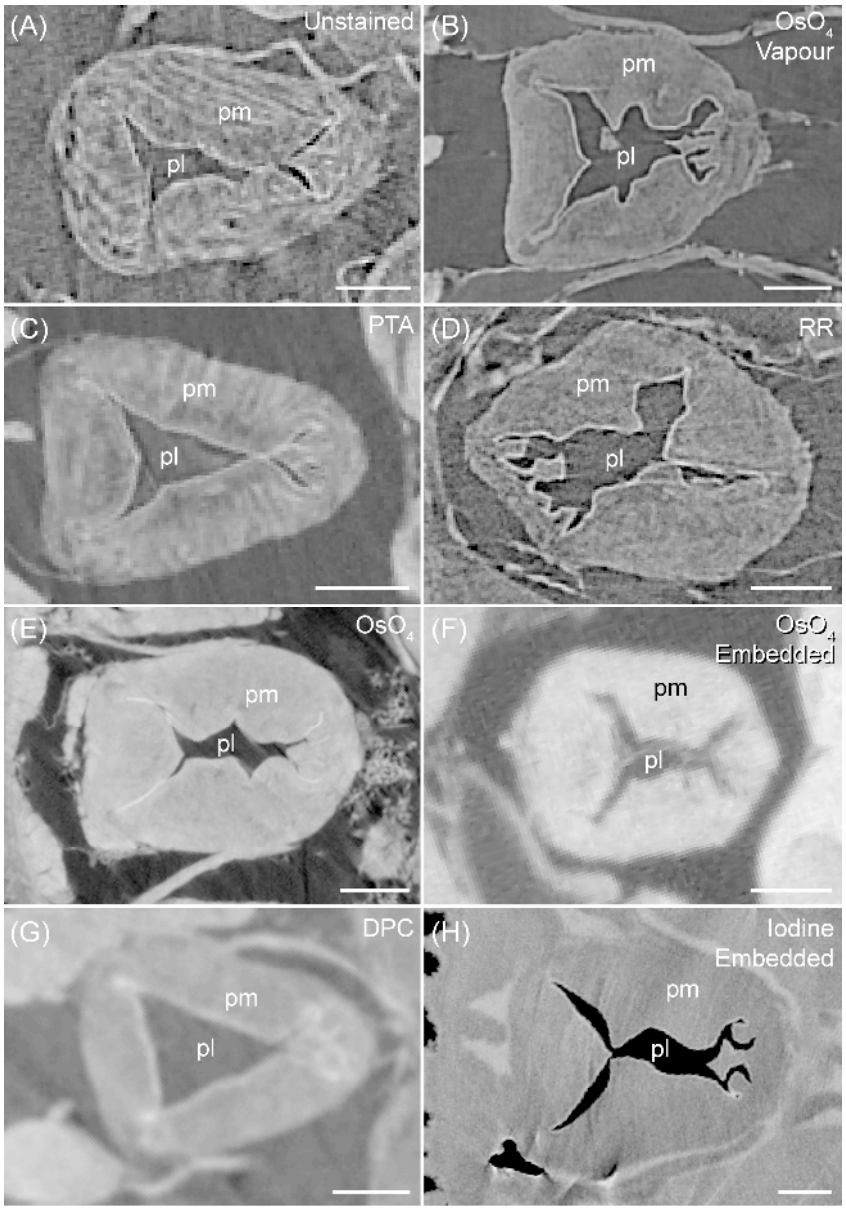

Comparative imaging of the onychophoran pharynx using different contrasting approaches.

167x240mm (300 x 300 DPI)

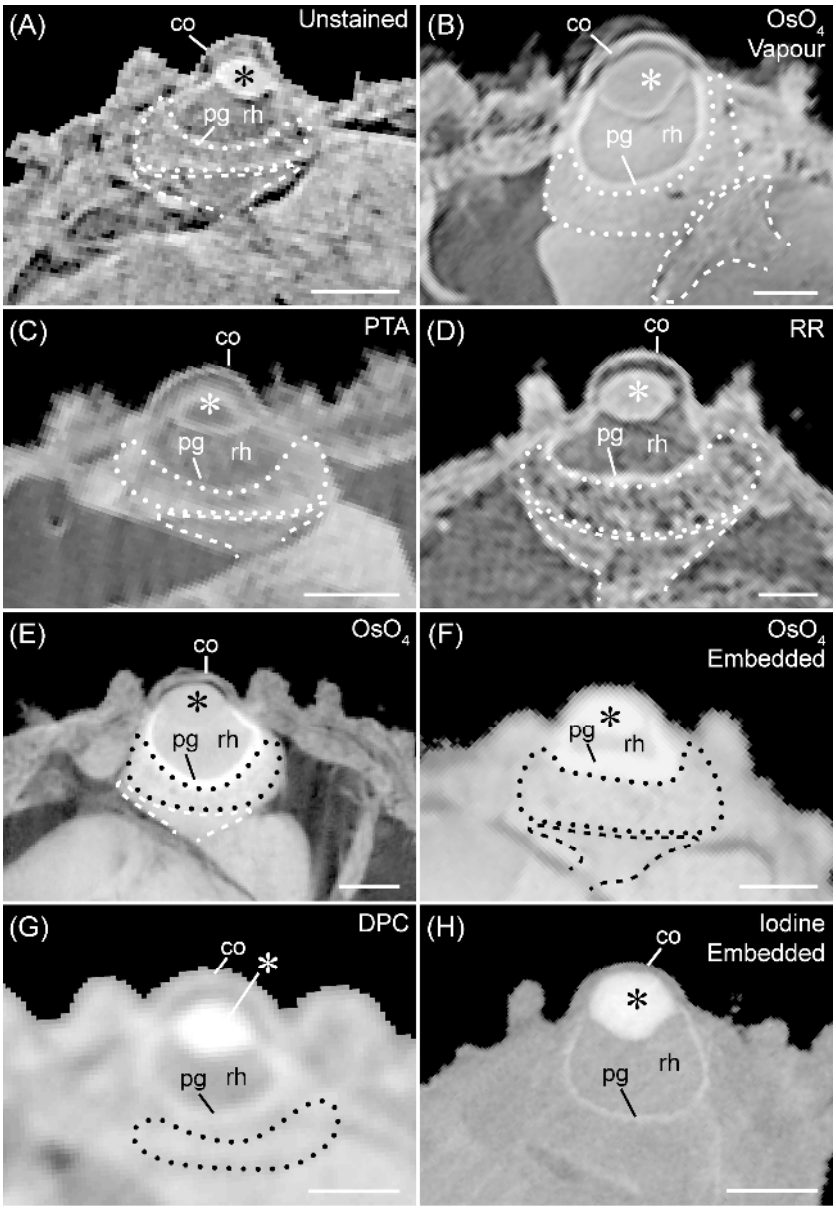

Comparative imaging of the onychophoran eye using different contrasting approaches.

167x242mm (300 x 300 DPI)

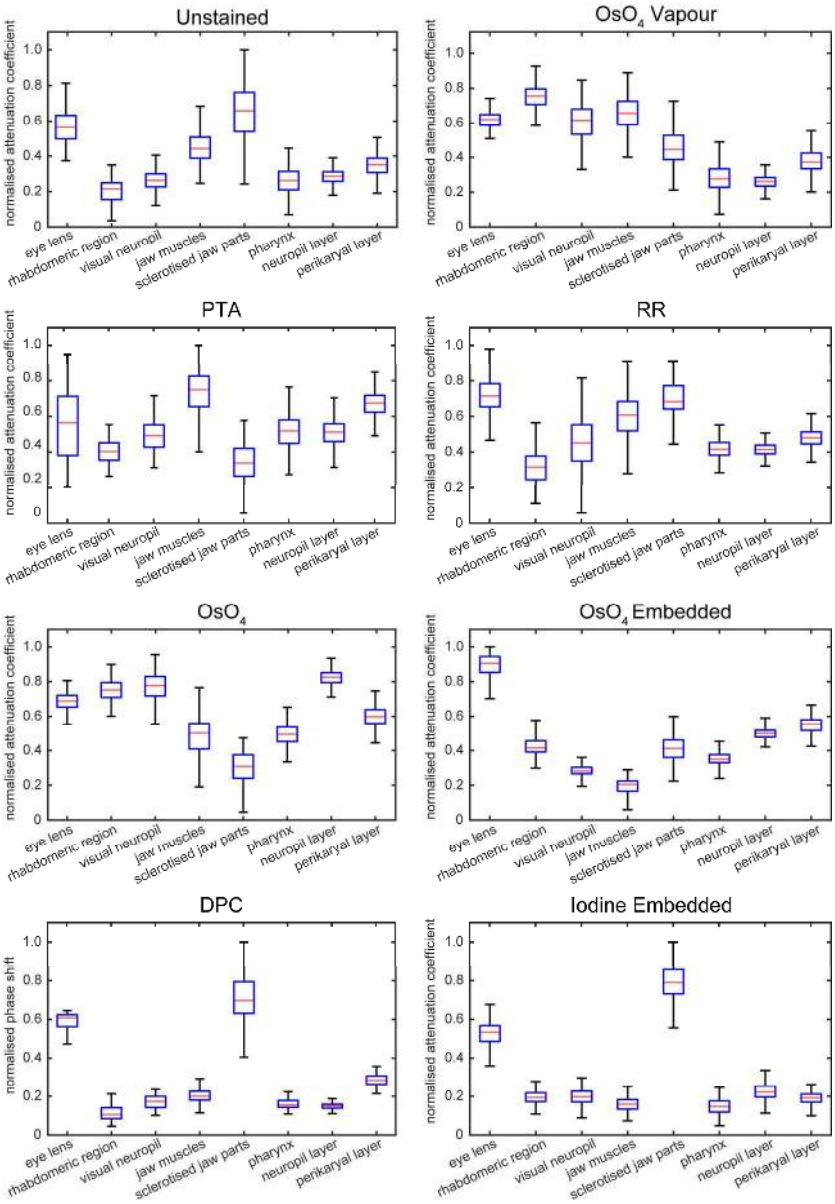

Quantitative comparison of grey value distribution within and among investigated organs in each dataset using box-and-whisker plots.

169x246mm (300 x 300 DPI)